

Celestial body irradiance determination from an underfilled satellite radiometer: application to albedo and thermal emission measurements of the Moon using CERES

Grant Matthews

Science Systems and Applications Inc., 1 Enterprise Parkway, Suite 200, Hampton, Virginia 23666, USA

*Corresponding author: grant.matthews-1@nasa.gov

Received 24 April 2008; revised 15 July 2008; accepted 16 July 2008;
posted 17 July 2008 (Doc. ID 95431); published 18 September 2008

The Clouds and the Earth's Radiant Energy System (CERES) is a program that measures the Earth radiation budget (ERB) from two polar orbiting satellite platforms. CERES radiometers are designed to make stable broadband measurements of scattered solar and emitted thermal radiative flux leaving Earth with an accuracy of 1% or better. Using versatile and programmable scan modes, it is also possible for every CERES instrument to view the Moon on each orbit. However, until now, it has not been possible to derive absolute measurements of lunar irradiance using CERES because the Moon's disk fills only 10% of the telescope field of view. This work presents a method of integrating CERES raster-scan data in order to obtain a measurement of the average scattered solar and emitted thermal radiance from the entire lunar disk. The technique results in excellent agreement between CERES instruments on different satellites as to lunar albedo and emitted thermal flux. The average broadband Moon albedo is measured by CERES at a value of 0.1362 ($\pm 2\text{--}3\%$) when normalized to a static lunar phase angle of 7° using the U.S. Geological Survey lunar irradiance Robotic Lunar Observatory model. The method for the first time also yields very accurate measurements of the thermal irradiance emitted from the Moon. These suggest an average long-wave flux of 977 W m^{-2} ($\pm 2\text{--}3\%$ at 7° phase), implying an approximate mean surface temperature of around 92°C . Statistical analysis on available data suggests that a CERES instrument performing monthly lunar measurements could utilize the Moon as a stability target and reduce calibration drifts to 0.3% per decade or less within an instrument's lifetime. Given the success of the technique, a solar calibration system is proposed that will allow precise tracking of an ERB instrument's optical degradation using the Sun. © 2008 Optical Society of America

OCIS codes: 040.0040, 280.0280, 010.0280, 040.6808, 120.6085, 350.1270.

1. Introduction

For some time the Moon has been successfully used by space-based Earth observing instruments^[1,2] as a radiative target to maintain calibration stability in scattered solar channels. The average reflectivity or “albedo” of the entire lunar surface is believed to remain constant at a level better than $10^{-8}\%$ per dec-

ade [3]. Monthly views of the Moon hence allow space-based photodiode gains to be adjusted, yielding excellent stability to Earth observation measurements. However, the precise figure of broadband lunar albedo has never been measured from space (as photodiodes are narrowband detectors and, hence, cannot be used to estimate broadband albedo with high accuracy).

The Clouds and the Earth's Radiant Energy System (CERES [4]) is a satellite program monitoring global Earth radiation budget (ERB) parameters

from space on the polar-orbiting Terra and Aqua satellite platforms. Flight models one and two (FM1 and FM2) operate on Terra while models three and four (FM3 and FM4) are on Aqua. CERES design specifications called for an absolute accuracy of 1% in measurements of short-wave (SW) Earth radiance (between 0.2 and $5\mu\text{m}$) and 0.5% for emitted thermal long-wave (LW) radiance ($5 < \lambda < 200\mu\text{m}$). CERES instruments are, to date, the most accurate Earth observing radiometers flown in space and do have the capability to view the Moon on every one of the Terra or Aqua Sun-synchronous orbits. However, the CERES field of view is approximately ten times larger than the extent of the lunar disk seen from low Earth orbit. Also, each CERES detector has a nonuniform spatial response within its field of view and a finite time response [5]. This complicates attempts to measure absolute lunar radiance directly, as is done for the ERB. This study details a new technique that enables CERES to make measurements of lunar radiance with absolute accuracy comparable to that obtained from overfilled Earth scenes. It utilizes new experimental calibration parameters derived based on the spectral darkening studies [6–8] for the CERES instruments, which were designed to account for in-flight contamination effects. These have the advantage that, by using deep convective cloud (DCC) albedo as a constant stability metric, calibration drifts in CERES measurements should be significantly reduced. The work is further aided because here all four instruments are calibrated to measure the same DCC albedo value; hence, they should be on a common SW radiometric scale.

2. CERES Instrument and Calibration Parameters

Each CERES instrument is a scanning radiometer with three coaligned channels. These are the SW telescope, which uses a quartz fused silica filter to select radiance in the range of $0.2 < \lambda < 5\mu\text{m}$. A window (WN) channel uses a zinc sulfide–cadmium telluride filter to select only thermal radiance in a specific region ($8 < \lambda < 12\mu\text{m}$). The ERB LW measurement is obtained using the third Total channel, which has no filtering optics so it receives all the energy in the range of $0.2 < \lambda < 200\mu\text{m}$. Daytime thermal measurements are hence obtained after subtraction of the SW-channel signal from that of the Total channel (see Fig. 1 for example CERES-channel spectral responses). The nonflat spectral nature of each telescope does require that the raw measurement be “unfiltered” [9], where Modtran spectra of the scenes involved are used to compensate for the telescope response variation in spectral shape.

Each CERES channel uses a thermistor bolometer detector that measures radiance by converting photon energy into heat once absorbed. Equation (1) gives a complete representation of how the voltage output of a CERES channel relates to the radiant input $L(\lambda, \theta, \phi, t)$ at time t :

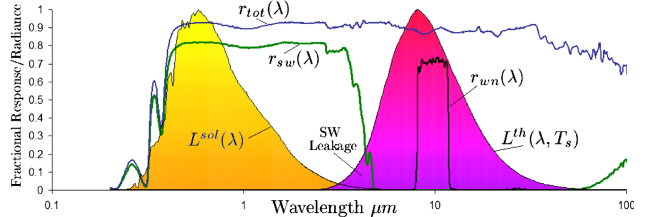


Fig. 1. (Color online) Three CERES-channel spectral responses plotted with scattered solar and emitted thermal lunar spectra.

$$V(t) = g \int_{-\infty}^t [\alpha_1 \eta_1 \exp(-\alpha_1(t-t')) + \alpha_2 \eta_2 \exp(-\alpha_2(t-t'))] \times \int_0^{2\pi} P(\theta, \phi) \times \int_0^{200} r(\lambda) L(\lambda, \theta, \phi, t') d\lambda d\Omega dt', \quad (1)$$

where g is a constant that gives the voltage output of the detector per unit quantity of heat energy converted in the thermistor. $r(\lambda)$ is the spectral response of the CERES channel that gives the fraction of incident radiance at wavelength λ , which is converted to heat energy within the detector (this is measured in the ground calibration and updated in-flight for this study using the spectral darkening work [6–8]). $P(\theta, \phi)$ is the telescope field-of-view response, often referred to as a point-spread function (PSF [10]). Wavelength-dependent broadening of the PSF due to diffraction is assumed to be minimal; hence, $P(\theta, \phi)$ is not represented as a function of λ . As thermal detectors, the CERES bolometers have a finite time response to energy input. In the case of CERES instruments, this results in a fast and slow time response of the detector [5]. The first and fastest response has a time lag of around 8 ms (α_1^{-1}) and represents about 99% of the signal (i.e., $\eta_1 \approx 0.99$). However, it is known that the detectors also have a slower second-time constant due to noninfinite thermal mass of the detector mountings [Fig. 2(a)]. This results in a further 1% rise ($\eta_2 \approx 0.01$, $\eta_1 + \eta_2 = 1$) in the detector signal that occurs with a time constant of around 300 ms [α_2^{-1} , see Fig. 2(b)]. In Earth-viewing data, this second-time constant effect is compensated for by using a recursive filter [11] that uses the current and previously sampled digital counts to numerically remove the long exponential drift.

For this study it is helpful to briefly consider the calibration measurement of the CERES-channel radiometric gain. This is done using a blackbody or lamp calibration source of known radiant output $L^c(\lambda)$ and a uniform spatial extent that overfills the CERES-channel telescope field of view. In ground calibration the CERES telescope scans onto the source and stares for several seconds, ensuring that both first- and second-time constant effects have a period sufficiently long to fully react. Source uniformity and calibration long stare (i.e., $L(\lambda, \theta, \phi, t) = L(\lambda)$, $t \rightarrow \infty$) allows Eq. (1) to be considerably simplified as

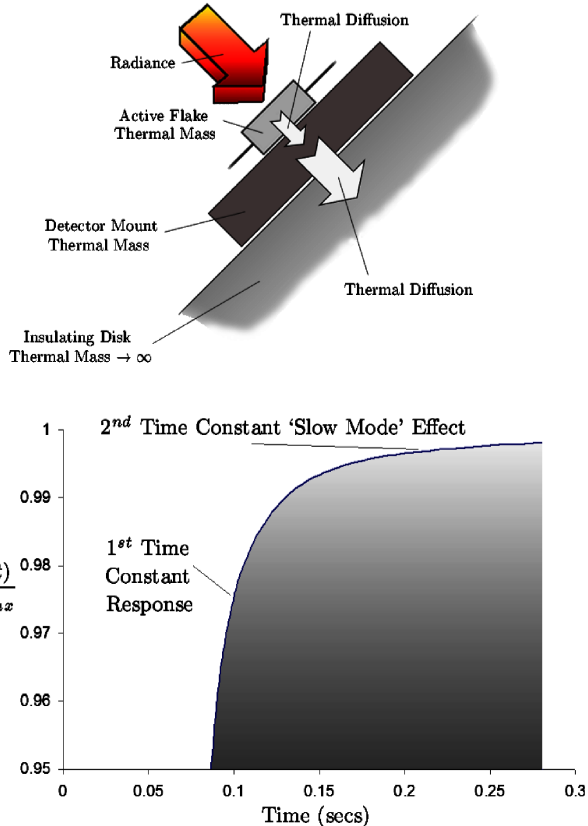


Fig. 2. (Color online) (a) Diagram illustrating physical cause of CERES bolometer flake fast and slow time response. Fast response due to heat flow to detector mount, slow response due to heat flow from mount to insulating disk. (b) Example of detector output when scanning onto stationary radiance target or step function where first- and second-time constant effects are apparent.

Eq. (2). Since the source radiance and telescope spectral response are known, the CERES-channel radiometric gain G is found using Eq. (3):

$$V_c(\infty) = g \int_0^{2\pi} P(\theta, \phi) d\Omega \times \int_0^{200} r(\lambda) L^c(\lambda) d\lambda, \quad (2)$$

$$G = \frac{V_c(\infty)}{\int_0^{200} r(\lambda) L^c(\lambda) d\lambda} \quad (3)$$

$$= g \int_0^{2\pi} P(\theta, \phi) d\Omega. \quad (4)$$

This gain value can hence be used, as in Eq. (6), to convert detector counts when viewing the Earth into measurements of unfiltered radiance from scene i :

$$f_i = \frac{\int_0^{200} r(\lambda) L^i(\lambda) d\lambda}{\int_0^{200} L^i(\lambda) d\lambda}, \quad (5)$$

$$\int_0^{200} L^i(\lambda) d\lambda = \frac{V_i(t)^*}{G \times f_i}. \quad (6)$$

The filtering factor f_i is calculated using the spectral response and a Modtran spectrum for the particular Earth scene i . Note that, in the production of ERB data, the unfiltering [9] is not done exactly as Eq. (6) suggests since it would require generation of a Modtran spectrum for every footprint (instead, regression coefficients are used based on comparing Modtran estimates of unfiltered versus filtered radiance for a range of scenes). However, the inversion form of Eq. (6) is more practical for this study since the lunar spectrum shape will not vary as much as that for Earth scenes. The unfiltering described in Subsection 3.C is, however, designed to closely mirror that done in production. The asterisk in $V_i(t)^*$ indicates that the detector output (for ERB data only) has been through the recursive filter [11] that compensates for the second-time constant effect. Importantly, this gain value can be applied in Eq. (6) only if the CERES telescope field of view is overfilled with radiance.

The CERES field of view is $1.3^\circ \times 2.6^\circ$ in order to obtain a 25 km sized footprint when viewing the Earth at nadir. As shown in Fig. 3(b), if the CERES telescope is aligned to view the Moon, the lunar radiance fills only 10% of the PSF. Such extreme underfilling of the CERES field of view and lack of known precise PSF shape $P(\theta, \phi)$ means that the standard inversion of Eq. (6) cannot be used to derive measurements of lunar radiance. Furthermore, the finite time response of CERES bolometers will add additional complications to any attempt to derive lunar radiance from a fast CERES scan across the Moon.

3. Use of Lunar Raster-Scan Data

A. Theoretical Basis

Originally intended for purposes of mapping PSF shape $P(\theta, \phi)$, the CERES instruments have begun performing regular raster scans of the Moon. These are obtained at sunrise for the Terra instruments and sunset for those on Aqua (to avoid telescope exposure to the ram direction and the degradation it causes [12]). The elevation scan head is held fixed while the azimuth of the instrument is rotated back and forth so the Moon zigzags through the telescope field of view, as shown in Figs. 3(a) and 3(b). The detector output $V_m(t)$ from raster-scan data [Fig. 3(c)] can be mathematically represented as

$$H(t) = \alpha_1 \eta_1 \exp(-\alpha_1 t) + \alpha_2 \eta_2 \exp(-\alpha_2 t), \quad (7)$$

$$M(\theta, \phi) = \int_0^{200} r(\lambda) L^m(\lambda, \theta, \phi) d\lambda, \quad (8)$$

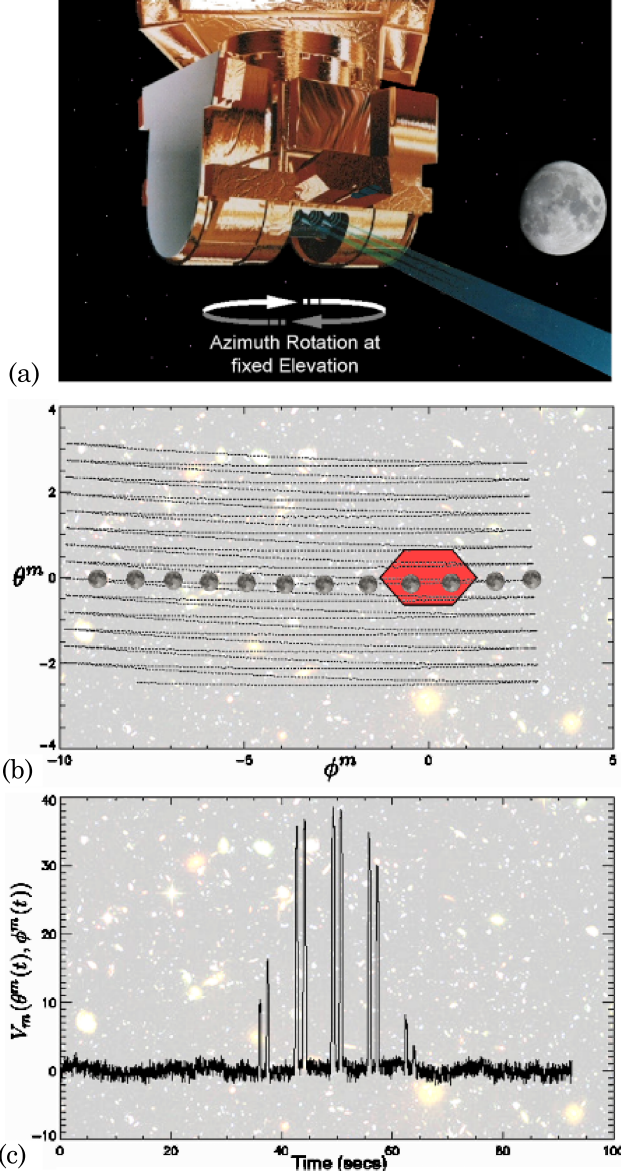


Fig. 3. (Color online) (a) CERES instrument in fixed elevation rotating azimuth lunar raster-scan mode. (b) Lunar azimuth and elevation angles during CERES raster scan (red area is telescope field of view). (c) Example CERES SW detector output during lunar raster scan. Hubble image credit: NASA.

$$V_m(\theta^m(t), \phi^m(t)) = g \int_{-\infty}^t H(t-t') \int_0^{2\pi} P(\theta, \phi) \\ \times M(\theta - \theta^m(t'), \phi - \phi^m(t')) d\Omega dt', \quad (9)$$

where $H(t)$ is the impulse response of the CERES bolometer [5] and $L^m(\lambda, \theta, \phi)$ is the spectrally and spatially resolved radiance from the Moon. Equation (9) shows how the detector output is the result of a convolution in time and angular space between

the impulse response $H(t)$, the PSF $P(\theta, \phi)$, and the filtered lunar radiance $M(\theta, \phi)$. This allows use of the mathematical property that the integral of a function, which is itself the convolution of multiple functions, gives the product of each function's integral:

$$Z = \int_{-\infty}^{\infty} \int_{-\infty}^t X(t') Y(t-t') dt' dt \quad (10)$$

$$= \int_{-\infty}^{\infty} X(t) dt \times \int_{-\infty}^{\infty} Y(t) dt. \quad (11)$$

It is, therefore, possible to use the Eq. (13) representation of an integral of CERES lunar raster-scan data over all angular space:

$$F_m = \int_0^{2\pi} V_m(\theta^m, \phi^m) d\Omega \quad (12)$$

$$= g \int_0^{2\pi} P(\theta, \phi) d\Omega \times \int_0^{\infty} H(t) dt \times \int_0^{2\pi} M(\theta, \phi) d\Omega, \quad (13)$$

$$\int_0^{\infty} H(t) dt = 1, \quad (14)$$

$$g \int_0^{2\pi} P(\theta, \phi) d\Omega = G, \quad (15)$$

$$F_m = G \int_0^{2\pi} M(\theta, \phi) d\Omega. \quad (16)$$

So when the integration of Eq. (12) is performed on CERES detector output during a lunar raster scan, the result must be the radiometric gain G [Eqs. (4) and (5)] multiplied by the disk integrated filtered radiance from the Moon [Eq. (16)]. If R_{eq} and R_{pol} are the equatorial and polar radii of the Moon (1738.14 and 1735.97 km) and D_{sm} is the satellite–Moon distance, Eq. (17) then gives the angular extent of the Moon. That can be used to give the mean filtered radiance K , leaving the lunar disk:

$$\Delta\Omega_m = 2\pi \left(1 - \left(1 - \frac{R_{eq} R_{pol}}{D_{sm}^2} \right)^{\frac{1}{2}} \right), \quad (17)$$

$$K = \frac{F_m}{G \times \Delta\Omega_m}. \quad (18)$$

This accounts for the lack of precise knowledge on PSF shape and detector time response. It also gives the advantage that, by integrating over thousands of samples, the signal to noise of K is significantly increased [note in Fig. 3(c) that the lunar radiance produces a small signal from the SW detector of around 35 counts, compared to a 1000 count signal from a typical Earth scene].

B. Accounting for Lunar Phase Variance

Each operational CERES instrument currently performs raster scans of the Moon at least once every calendar month (typically when the lunar-phase angle is near 7°). These scans are done throughout the day on multiple orbits. To maximize the signal-to-noise ratio in the result K , the integration of Eq. (12) is performed on the entire day's worth of data. However, the orbital motion of the Moon serves to alter the phase angle among the Sun, Moon, and satellite during a 24 h period by several degrees. It is known that, for these low phase angles, the brightness of the Moon can vary significantly, causing a large drift in the CERES measurement during the day. Hence, prior to the integration of Eq. (12), the CERES counts need to be normalized to compensate for variations in lunar brightness. The U.S. Geological Survey (USGS) lunar calibration program has acquired an extensive database of lunar images at 32 discrete wavelengths in the solar reflectance range. A model has then been developed [13] that is capable of providing lunar irradiance at wavelengths for all phase/libration geometries. This lunar irradiance model, the Robotic Lunar Observatory (ROLO) [13] can, therefore, estimate the disk equivalent reflectance A_k at 32 discrete wavelengths for each raster slice that CERES takes through the Moon. Use of all 32 of these wavelengths covers the wavelength range of $0.35 < \lambda < 2.38 \mu\text{m}$. The result, A_k , is then interpolated and extrapolated to the 10 nm resolution result $A(\lambda)$ that covers the CERES SW bandpass. A model estimate, $L_{p,q}^{\text{sol}}(\lambda)$, can then be generated, giving the spectral shape of the scattered solar lunar SW flux measured by CERES on raster-scan slice q and occurring on day p :

$$\int_0^5 I(\lambda) d\lambda = 1, \quad (19)$$

$$L_{p,q}^{\text{sol}}(\lambda) = \left(\frac{1365}{1361} \right) \times I(\lambda) \times A^{p,q}(\lambda), \quad (20)$$

$$U_p = \frac{S_p}{N_p} \sum_{q=1}^{N_p} \int_0^5 L_{p,q}^{\text{sol}}(\lambda) d\lambda, \quad (21)$$

where $I(\lambda)$ is a solar reference spectrum normalized so its integral is unity [Eq. (19), a constant SORCE (Solar Radiation and Climate Experiment) [14] measured spectrum is used, assuming solar UV output variations have little effect on total energy scattered from the lunar surface]. S_p is the total solar irradiance at the lunar surface on day p (corrected to current Moon–Sun distance from the SORCE instrument data set [14]). The use of SORCE data in this study also requires the adjustment of the ROLO model albedo by the factor 1365/1361 in Eq. (20). This is because ROLO model results were derived using an assumed solar constant of 1365 W m^{-2} . In this paper, albedo results will be adjusted to a figure of 1361 W m^{-2} in accordance with the SORCE data set. Equation (21), therefore, uses the model to estimate the average SW flux scattered from the lunar surface on day p to arrive at the CERES instrument.

The “filtered flux,” or amount of scattered SW that is absorbed in the CERES bolometer on each slice, is then estimated by Eq. (22). Use of this in the denominator of Eq. (24) adjusts the SW-channel output such that the integral over all solid angles yields the average “filtered radiance” absorbed in the SW detector during the day. Such an adjustment for lunar brightness is not deemed necessary for the Total and WN telescope signal integration [Eqs. (25) and (26)]. This is because the Moon's thermal radiance variation is assumed to be linear and to dominate over the scattered solar in these channels:

$$\omega_{p,q} = S_p \int_0^5 r_{\text{sw}}(\lambda) L_{p,q}^{\text{sol}}(\lambda) d\lambda, \quad (22)$$

$$W_p = \frac{1}{N_p} \sum_{q=1}^{N_p} \omega_{p,q}, \quad (23)$$

$$K_{\text{sw}}^p = W_p \int_0^{2\pi} \frac{V_{\text{sw}}^{p,q}(\theta^m, \phi^m)}{\omega_{p,q} \times G_{\text{sw}} \times \Delta\Omega_m^{p,q}} d\Omega, \quad (24)$$

$$K_{\text{tot}}^p = \int_0^{2\pi} \frac{V_{\text{tot}}^{p,q}(\theta^m, \phi^m)}{G_{\text{tot}} \times \Delta\Omega_m^{p,q}} d\Omega, \quad (25)$$

$$K_{\text{wn}}^p = \int_0^{2\pi} \frac{V_{\text{wn}}^{p,q}(\theta^m, \phi^m)}{G_{\text{wn}} \times \Delta\Omega_m^{p,q}} d\Omega. \quad (26)$$

The results K_{sw}^p , K_{tot}^p , and K_{wn}^p , therefore, represent CERES measurements of filtered lunar radiance averaged over all phase angles at which the instrument viewed the Moon that day.

C. Unfiltering CERES Lunar Radiance

To unfilter the result K , an estimate of the lunar thermal radiance spectral shape is required, as well as the scattered solar spectrum from Eq. (20). To do this, Apollo LW reflectivity data [15] are used to give the emissivity $\epsilon(\lambda)$ of the lunar soil [emissivity $\epsilon(\lambda) = 1 - \text{reflectivity}(\lambda)$]. This is then combined with a Planck blackbody radiance curve $B(\lambda, T_s)$ for lunar surface temperature T_s to estimate the thermal spectrum, as in Eq. (27). At no point in this study is the extrapolation of Apollo soil emissivity and single temperature T_s to the entire lunar surface assumed to be an accurate way to determine thermal spectral shape (it is, however, necessary and, as discussed later, has little effect on quality of the LW flux result). Example scattered solar and emitted thermal spectra are shown in Fig. 1 along with typical CERES-channel spectral responses. Since the CERES Total channel is equally sensitive to scattered solar and thermal radiance, the model must also be used to estimate the filtered flux quantity Γ_p . This is needed because it tells of the amount of the filtered K_{tot}^p result that is caused by reflected sunlight:

$$L^{\text{th}}(\lambda, T_s) = B(\lambda, T_s) \times \epsilon(\lambda), \quad (27)$$

$$\Gamma_p = \frac{S_p}{N_p} \sum_{q=1}^{N_p} \int_0^5 r_{\text{tot}}(\lambda) L_{p,q}^{\text{sol}}(\lambda) d\lambda. \quad (28)$$

An important consideration for CERES lunar measurements is the high temperature of the lunar surface. The illuminated Moon's temperature can exceed 100 °C, far warmer than any of the Earth scenes from which CERES was designed to measure radiance. As illustrated in Fig. 1, this will result in significant "thermal SW leakage" of infrared lunar radiance that can pass through the quartz filter. For Earth data unfiltering [9], a nighttime training of the CERES WN channel is used to estimate this leakage based on the CERES SW-channel signal at night (which is typically a couple of counts or <0.2% of the signal). However, such training coefficients cannot be accurately used to give the lunar SW leakage because the Moon's surface is so much warmer than that of the Earth when illuminated. Nor is it possible to perform a similar training of the WN channel using a "dark" Moon because, when not in direct sunlight, its temperature is incredibly low. A solution is to rely on an iterative matching of the difference in Total and SW-channel signals with the theoretical figure generated for variable surface temperatures, as in Eq. (29):

$$K_{\text{tot}}^p - \frac{\Gamma_p K_{\text{sw}}^p}{W_p} \equiv \int_0^{200} r_{\text{tot}}(\lambda) L^{\text{th}}(\lambda, T_s) - \frac{\Gamma_p \times r_{\text{sw}}(\lambda) L^{\text{th}}(\lambda, T_s)}{W_p} d\lambda, \quad (29)$$

$$h_p = \frac{\pi \int_0^{200} L^{\text{th}}(\lambda, T_s^p) d\lambda}{\int_0^{200} r_{\text{tot}}(\lambda) L^{\text{th}}(\lambda, T_s^p) d\lambda}, \quad (30)$$

$$d_p = \frac{\pi \int_0^{200} L^{\text{th}}(\lambda, T_s^p) d\lambda}{\int_0^{200} r_{\text{wn}}(\lambda) L^{\text{th}}(\lambda, T_s^p) d\lambda}, \quad (31)$$

$$R_p^{\text{SW}} = \frac{\pi U_p}{W_p} \times K_{\text{sw}}^p - \frac{\pi U_p}{W_p} \int_0^{200} r_{\text{sw}}(\lambda) L^{\text{th}}(\lambda, T_s^p) d\lambda, \quad (32)$$

$$R_p^{\text{LW}} = h_p \times \left(K_{\text{tot}}^p - \frac{\Gamma_p}{\pi U_p} \times R_p^{\text{SW}} \right), \quad (33)$$

$$R_p^{\text{WN}} = d_p \times K_{\text{wn}}^p. \quad (34)$$

Hence, the Moon's surface temperature T_s is iterated until the equality of Eq. (29) becomes true, at which point it becomes the estimate on day p of the average lunar temperature T_s^p . Then the SW thermal signal can be subtracted [Eq. (32)] and the results unfiltered to give SW and LW lunar irradiance measurements R_p^{SW} and R_p^{LW} (thermal leakage from the Moon is typically 5–7% of the K_{sw}^p signal). The WN-channel filtered radiance can also be inverted to give a measure of thermal flux R_p^{WN} , as in Eq. (34). This is, however, a far less accurate result than that from the LW channel as it relies on a narrowband measurement and requires accurate knowledge of the lunar thermal spectrum. The "flat" nature of the Total-channel spectral response in the LW (Fig. 1) means that uncertainty in the knowledge of lunar soil emissivity and geographic variation in surface temperature will have little effect on the accuracy of the unfiltering factor h_p . It will, however, have a greater effect on the accuracy of the estimate of T_s^p and, hence, the thermal leakage of the SW channel. In all cases, the Moon is treated as a point source, enabling the CERES measurement of radiance K to be converted to irradiance with the simple factor of π .

The CERES instrument gains and the spectral responses used to invert lunar radiance are those derived based on the spectral-darkening studies [6–8]. These have been produced in preparation for the forthcoming CERES data release and are normalized to the SW Tropical Rainfall Measuring Mission (TRMM) DCC albedo radiometric standard [8]. This is important because these calibration parameters were designed to place all CERES SW measurements by different instruments onto a common radiometric scale. It should be noted, however, that at present they are not representative of an official release or edition of CERES data. Such parameters are held static for 2005 onward, assuming that new ram-avoidance

modes [12] keep CERES SW calibration stable to 0.2% or better.

4. CERES Lunar Irradiance Results

A. Irradiance Variation with Lunar Phase

Figure 4(a) shows SW irradiance measurements R_p^{SW} from all CERES instruments on the Terra and Aqua satellites made from 2003 until early 2008 (after adjustment for changes in solar irradiance using the factor $1361/S_p$). Only four measurements were available from FM4 because of the March 2005 failure of the SW channel. Also, plotted in black circles are the model results U_p that accompany each CERES measurement. This shows the excellent agreement between CERES and the model in the variation in lunar brightness with phase angle (as well as a typically slightly brighter waxing versus waning Moon).

Figure 4(b) then shows the corresponding thermal irradiance results R_p^{LW} and their variation with lunar phase. These, too, have been normalized to a solar irradiance of 1361 Wm^{-2} using a linear regression of the LW results R_p^{LW} against the solar input S_p :

$$R_p^{\text{LW}} = m \cdot S_p + c, \quad (35)$$

$$R_p^{\text{LW}'} = R_p^{\text{LW}} \times \left(\frac{m \times 1361 + c}{m \cdot S_p + c} \right), \quad (36)$$

where the regression coefficients m and c are derived separately for each instrument. These results show a very high thermal output of nearly 1000 Wm^{-2} from the lunar surface for low phase angles. If a further regression of these results is performed with the absolute phase angle ψ_p , a near linear decrease in output of around $-4 \text{ Wm}^{-2}/\text{degree}$ is observed:

$$R_p^{\text{LW}''} = a \cdot \psi_p + b, \quad (37)$$

$$R_p^{\text{LW}''''} = R_p^{\text{LW}''} \times \left(\frac{a \times 7 + b}{a \cdot \psi_p + b} \right). \quad (38)$$

Using these regression coefficients it is, therefore, possible to observe seasonal variations in lunar thermal output for a fixed-phase angle of 7° by adjusting the original LW results, as in Eq. (38). These results $R_p^{\text{LW}'''}$ are shown in Fig. 4(d) to display a near 60 Wm^{-2} seasonal variation in the Moon's thermal emission. This is reasonable compared to the slightly more than 90 Wm^{-2} variation in solar irradiance between winter and summer. As expected, the maximum emission occurs during northern hemisphere wintertime, when the Moon is closest to the Sun. The average retrieved surface temperature by the iteration from Subsection 3.C suggests the mean surface temperature of the Moon at 7° phase and solar irradiance

of 1361 Wm^{-2} is around 92°C . As stated earlier for the WN result, the accuracy of this retrieval is likely to be lower than that of the LW flux measurement since it assumes retrieved Apollo sample emissivity represents the entire lunar surface. However, the variation in thermal flux correlates well with the retrieved 6°C seasonal range in temperature T_s^p . The relative noise in the thermal measurements is significantly lower due to the LW signal being near to an order of magnitude greater than that of the SW channel.

For validation of this lunar radiance retrieval technique (as well as the proposed CERES calibration parameters), it is important to compare the average measurements obtained from the different instruments. Figures 4(a), 4(b), and 4(d) imply good agreement in the measurements of SW and LW lunar flux by the different CERES instruments on the Terra and Aqua platforms. However, as indicated by the model results in Fig. 4(a), the lunar albedo can vary significantly for a fixed-phase angle depending on lunar libration and observer selenographic position [13] (this scatter is real, natural variation). Hence, for SW interinstrument comparison, it is decided to normalize all SW results to a lunar phase and solar longitude of 7° , with observer selenographic latitude and longitude of zero (as used to display results in Fig. 8 of [13]). This geometry is used in the model to calculate the “fixed-phase” albedo $A^0(\lambda)$ at CERES wavelengths. Then, an estimate of lunar flux U_0 for these conditions is generated (remembering the model is based on a solar constant of 1365 rather than 1361 Wm^{-2}):

$$U_0 = 1365 \int_0^5 I(\lambda) \times A^0(\lambda) d\lambda, \quad (39)$$

$$\chi_p^{\text{SW}} = R_p^{\text{SW}} \times \frac{U_0}{1361 \times U_p}. \quad (40)$$

This enables normalization of all SW flux measurements to give the “fixed-phase” lunar albedo χ_p^{SW} from CERES using Eq. (40). Figure 4(c) shows that the result of this normalization for all four CERES instruments again gives excellent visual agreement on a lunar albedo of around 13.62%.

Figure 5(a) shows the average albedo χ^{SW} at static 7° phase along with the corresponding 95% confidence intervals from three CERES instruments (the FM4 instrument results are not shown due to lack of data to give statistical significance). The SW calibration parameters used in this study were intended to place all CERES instruments on a common SW radiometric scale [8] based on DCC albedo. Indeed FM2 and FM3 agree on lunar albedo well within confidence limits while FM1 measures the albedo slightly higher than the average 0.1362 value (with near statistical significance). As described earlier, this is likely due to increased uncertainty in the

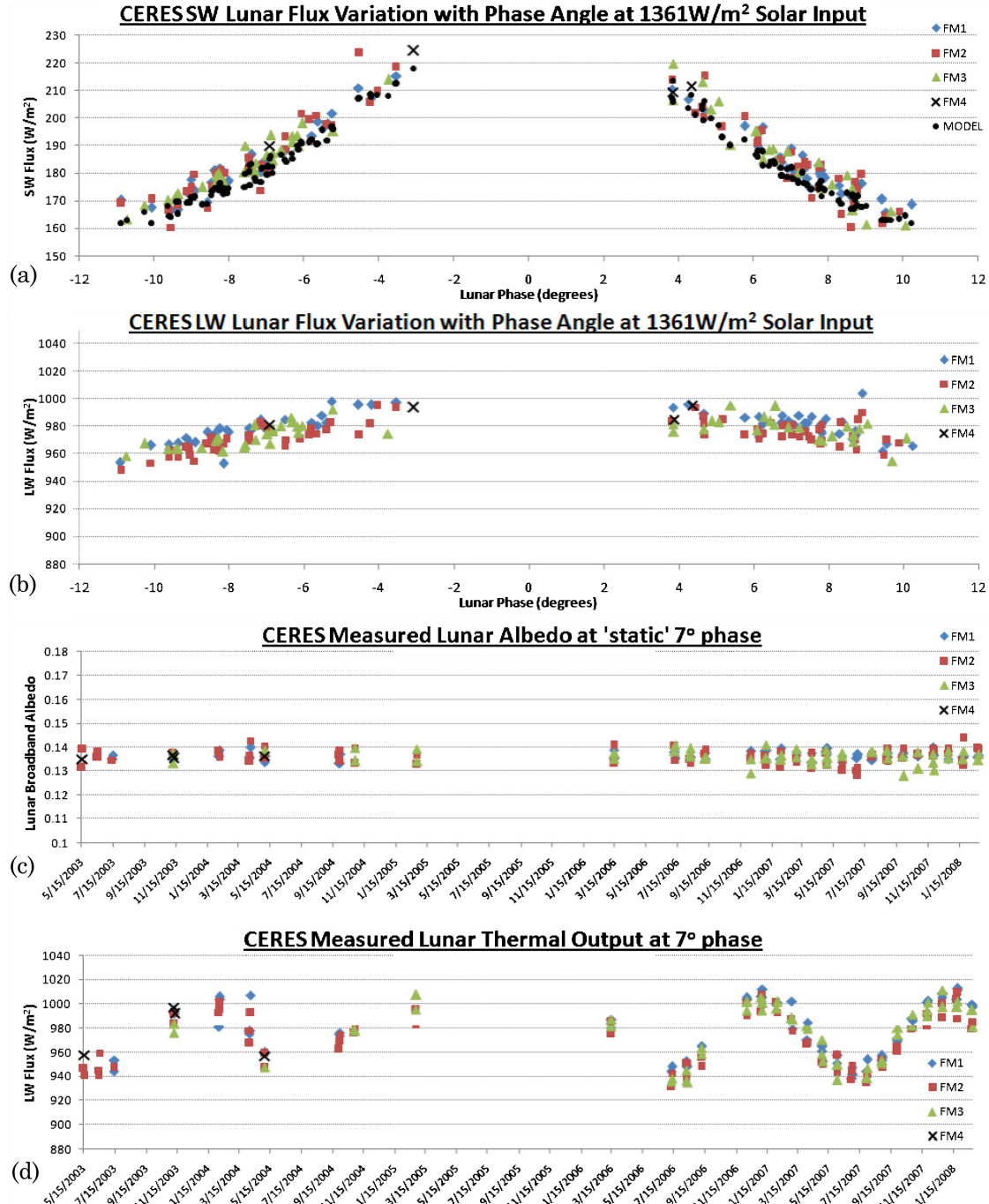


Fig. 4. (Color online) (a) CERES scattered solar flux measurements of the Moon at different phase angles. (b) CERES emitted thermal flux measurements of the Moon at different phase angles. (c) CERES measurements of lunar albedo at “static” 7° phase. (d) CERES measurements of lunar LW flux at 7° phase.

determination of thermal leakage for the SW channel (as well as differences between lunar and DCC spectra). However the FM1 value is well within the FM2 and FM3 statistical limits, giving overall confidence in this retrieval technique of lunar radiance using raster data.

Interinstrument comparisons of thermal flux will also require normalization to a constant state of both solar irradiance and phase. This is done using the re-

gression coefficients a , b , m , and c determined as in Eqs. (35) and (37) for both the LW and the WN results. The LW and WN fluxes are hence normalized to 7° phase and 1361 Wm⁻² solar input as in Eq. (41):

$$\chi_p^{\text{LW/WN}} = R_p^{\text{LW/WN}} \times \left(\frac{a \times 7 + b}{a \cdot \psi_p + b} \right) \left(\frac{m \times 1361 + c}{m \cdot S_p + c} \right). \quad (41)$$

The mission averaged thermal flux results χ^{LW} and χ^{WN} are shown for three instruments in Figs. 5(b) and 5(c), along with the corresponding 95% confidence intervals. The average thermal irradiance measured by all four instruments is 977 W m^{-2} . Figure 5(b) suggests there is statistical significance in the disagreement of lunar LW flux between FM1 and FM2. This is, however, to be expected because the technique of spectral balancing [7,8] was used to place FM1 and FM2 on a similar thermal radiometric scale for the average “allsky” Earth scene only. FM2 actually still consistently reads a 0.5–1% lower thermal flux than FM1 for warm scenes, such as tropical ocean and deserts (this is believed to be due to slight inaccuracies in knowledge of the Total-channel spectral response shape in the $5 < \lambda < 10 \mu\text{m}$ region, see [16]). Importantly, in Fig. 5(b) there is good agreement between all three measurements of lunar thermal flux within 1%. This is of particular relevance for CERES calibration validation as, thus far, no method has been developed to ensure Terra and Aqua LW measurements are on a common radiometric scale (while DCC albedo was used to place SW measurements by instruments on different satellites onto the same scale). Figure 5(b) implies such an adjustment may not be necessary; the good agreement between FM3 (Aqua) and FM2 (Terra) in the LW can be attributed to high stability and accuracy in the use of onboard blackbodies to update Total-channel gains.

Figure 5(c) indicates a statistically significant difference in the WN calibration between Terra (FM1 and FM2) and Aqua (FM3). As required by [8], FM1 and FM2 WN-channel calibration is near identical, while FM3 reads a higher thermal energy from the lunar surface. If deemed appropriate, these lunar measurements can be used to adjust the Aqua WN-channel gains and bring them onto the same radiometric scale as the Terra CERES units (FM1 and FM2, the Terra scale is preferable because the Aqua units are suspected of being subject to ground contamination prior to launch [8]). The WN-channel measurements of thermal flux are, in all cases, significantly higher than those measured by the CERES LW channels. As well as potential differences in WN- and Total-channel radiometric scales, this again is likely to be due to the inaccuracies in the assumed emissivity of lunar soil required in the inversion parameter d_m [Eq. (31)]. To confidently convert the narrowband WN-channel measurement into a broadband thermal flux, an accurate knowledge of the true average lunar disk emissivity and temperature distribution would be required.

B. CERES Calibration Stability Derived from Celestial Body Measurements

As mentioned earlier, the Moon has been successfully used as a stability target for Earth-viewing radiometers. In this section a brief analysis of the CERES lunar irradiance results from the FM3 instrument is performed to quantify what calibration stability can

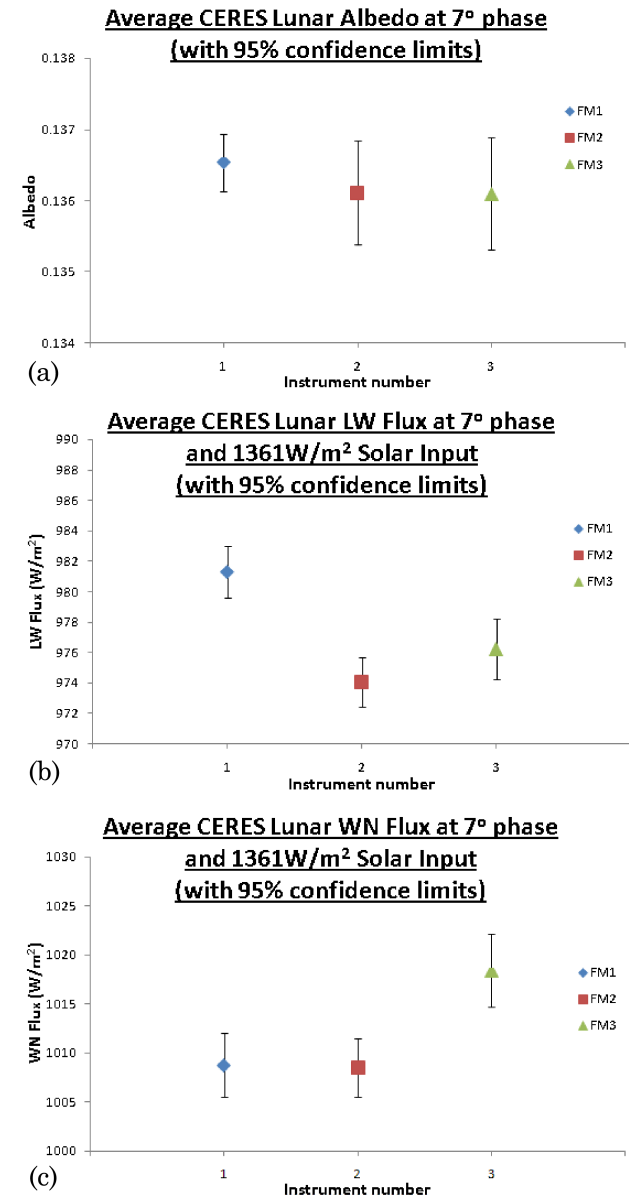


Fig. 5. (Color online) (a) Mission life averages and 95% confidence intervals of lunar albedo measurements by three different CERES instruments. (b) Mission life averages and 95% confidence intervals of lunar LW flux measurements by three different CERES instruments. (c) Mission life averages and 95% confidence intervals of lunar WN flux measurements by three different CERES instruments.

be obtained using the Moon. Figure 6 shows trends in static FM3 albedo and normalized LW/WN lunar flux. In all three cases, the trend magnitude is smaller than the 95% confidence in the slope, indicating that they have no statistical significance:

$$\sigma = \left[\frac{\sum(y_p - [\mu \times t_p + \nu])^2}{(n-2) \sum(t_p - \bar{t})^2} \right]^{\frac{1}{2}}. \quad (42)$$

Equation (42) is used to calculate the standard error of the slope μ , the regression of CERES lunar data y_p

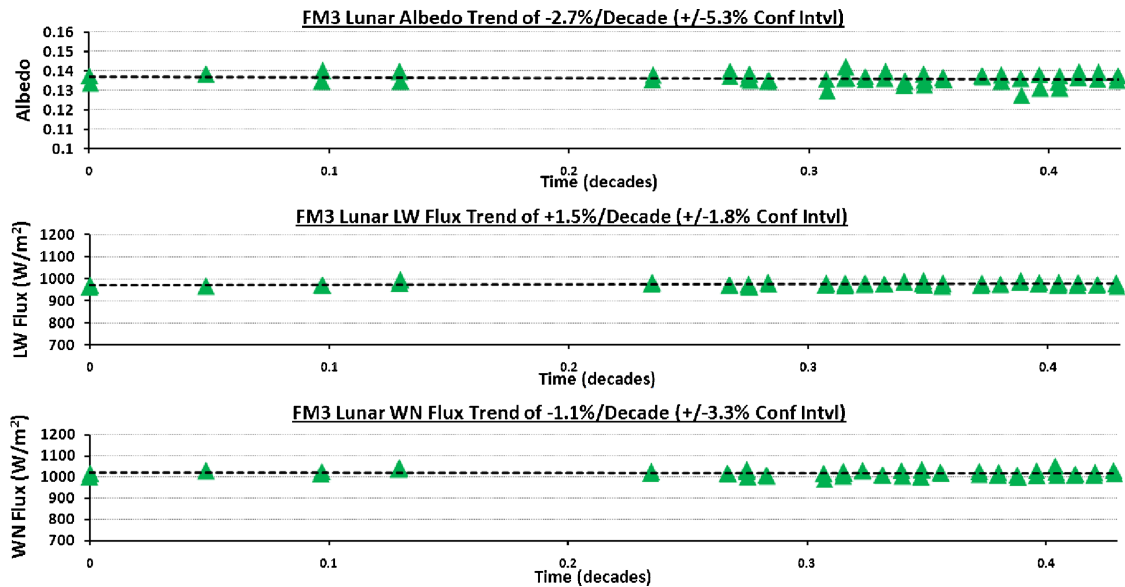


Fig. 6. (Color online) Current trends in FM3 measurements of SW, LW, and WN lunar irradiance.

against time t_p (with n as the number of measurements and ν as the regression intercept). However, assuming that the standard deviation of the available FM3 data represents the parent population for the whole mission, it is possible to calculate how the standard error of the slope will decrease as more lunar measurements are made. Recent studies [17] have called for measurements of the ERB to strive for a calibration stability of 0.3% per decade. If current and future CERES instruments perform two lunar calibrations every 29.5 days, then it can be estimated when the two sigma uncertainty of any slope in the lunar data will drop below the 0.3% threshold.

Figure 7 shows a prediction of the drop in standard error of trends from an “FM3-like” CERES instrument’s albedo (SW) and thermal (LW and WN) measurements of the Moon. The high thermal output of the illuminated lunar surface provides sufficient signal-to-noise ratio in the CERES LW measurement so that the 0.3% two sigma target is met after only six years. The WN channel also meets the target after nine years. Since both Terra instruments have operated for longer than eight years, this suggests the Moon can provide an excellent check on the stability of CERES onboard blackbodies (which are currently relied upon entirely to maintain stability of CERES LW measurements of the Earth).

For SW lunar measurements, it takes 12 years for the target climate stability goal to be met. This may be longer than the expected operational life of a CERES instrument or the satellite platform on which it sits. However, the one sigma 0.3% goal is indeed met after eight years, so lunar albedo measurements will provide an excellent check on the assumed stability of DCC albedo [6] (as well as a stable target metric with differing spectral content to both clouds and the onboard calibration lamps). It may also be possible for a CERES instrument to view

the Moon more frequently than twice per lunar cycle and, therefore, increase the stability of albedo data. This will, however, reduce the time available for collecting a continuous ERB data record so may not be practical for a solo CERES instrument.

Hence, present and future CERES instruments’ calibration stability could be greatly aided by use of regular lunar measurements and the techniques presented here. Also, new ERB instruments could perhaps be matched to current CERES radiometric scales using raster scans of the Moon.

However, given the lower signal in SW lunar results and the nature of the spectral darkening [6], on future CERES-like instruments it may still prove challenging to characterize degradation given only DCC and lunar albedo spectra as calibration metrics. This is because the vast majority of darkening appears to occur in the blue-UV part of the spectrum. Hence, given the success of the technique presented

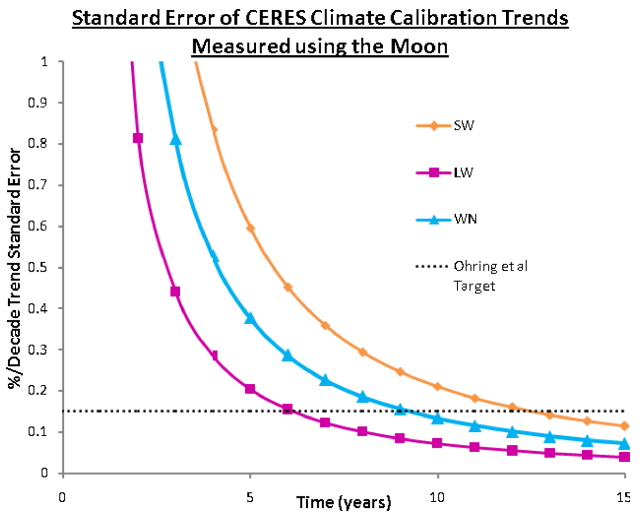


Fig. 7. (Color online) Prediction of drop in SW, LW, and WN lunar trend standard error compared to climate calibration stability goal.

here, a new design of solar calibration system for a space-based ERB radiometer is suggested in Fig. 8. The design requires the instrument to have no additional moving parts compared to the existing CERES units. As shown in Fig. 8(a), two additional telescopes for each SW and Total channel are recommended for addition to the rotating scan head. Ideally these telescopes and detectors should be identical in design to the Earth-viewing CERES channels (but if cost/power budgets are not sufficient, then narrowband detectors, such as photodiodes, should be adequate providing they have sufficiently linear responses). One of the two additional channels is equipped with a blue narrowband interference filter, while the other has a red filter incorporated into the optical train. The precise central wavelengths of these filters is open for discussion, but it is important that their bandwidth is sufficiently narrow to allow direct viewing of the Sun without saturating a CERES detector. 410 and 633 nm interference filters are suggested given the nature of contaminant transmission observed on existing CERES instruments [see Fig. 8(a)]. The final modification is that, for each new telescope, an additional and identical narrowband filter be positioned on the instrument casing (with the red filter under the SWICS and blackbodies and the blue optic just below the 0° elevation position, as in Fig. 8(b)].

For an instrument equipped with these modifications the solar calibration is then a three-step process. First, the additional telescope is positioned, such as in Fig. 8(b), and a raster scan of the Sun is performed in the same manner as for the Moon. The second step is to then perform a further raster scan of the Sun on the following orbit. However, this time the telescope is at the elevation position shown in Fig. 8(c) so that two filters are in the optical train. For each of these two steps an integration of the form of Eq. (12) is performed on the detector counts. The ratio of the integrals from steps two [Fig. 8(c)] and one [Fig. 8(b)] will hence tell of changes to absolute transmission of the filter attached to the instrument casing. The third and final step is for the Earth-viewing CERES telescope to perform a raster scan of the Sun through the narrowband filter with its transmission change now known [Fig. 8(d)]. This is to be performed on multiple orbits for both blue and red filters every month (ensuring that the telescopes avoid the ram direction exposure that is largely the cause of spectral darkening [6]). This will allow real-time tracking of changes to the absolute throughput of the Earth-viewing telescopes at two specific wavelengths. The spectral responses can, therefore, be updated accordingly using an appropriate spectral-darkening curve [6]. The success of the proposed device relies, of course, on continued monitoring of the solar output and stability in the bandwidth of the narrowband filters. If knowledge of the filter spectral transmission is sufficiently accurate, the technique will also allow a check on the absolute SW radiometric scale of future ERB instruments

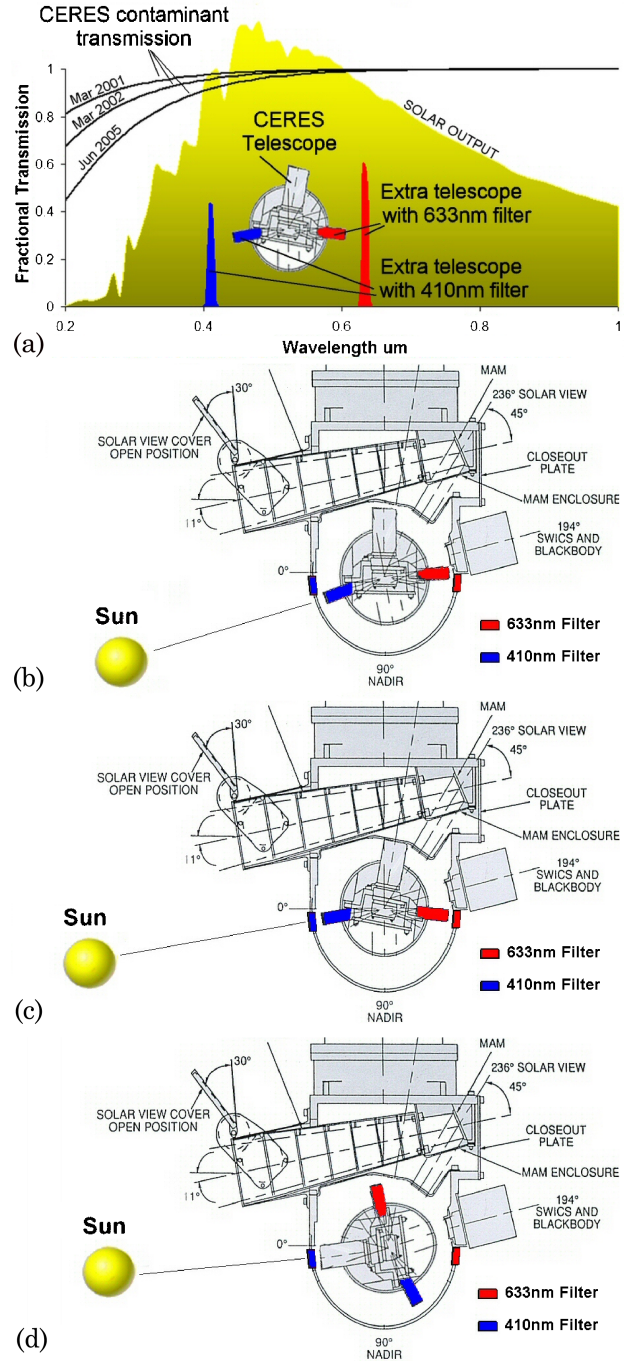


Fig. 8. (Color online) (a) Graph of CERES spectral-darkening contaminant transmission along with blue and red narrowband filter throughput proposed for addition to a future ERB telescope system. (b) Extra-narrowband telescope performs raster scan of the Sun. (c) Extra-narrowband telescope performs raster scan of the Sun through second filter fixed to the scan frame. (d) Earth viewing broadband telescope performs raster scan of the Sun through narrowband filter.

(i.e., because the precise energy throughput of the filter will also be known).

5. Summary

This paper details a method of determining disk-integrated radiative output from a celestial body whose

angular extent severely underfills a space-based telescope. The technique was applied to raster-scan data of the Moon by the CERES instruments on the Terra and Aqua platforms.

The CERES SW data was normalized to account for lunar phase and libration changes using simulations of disk-integrated albedo from the ROLO [13] model. The resulting CERES SW flux measurement variation with lunar phase agrees well with the model results. When standardized to a static lunar phase of 7° , the different CERES instruments agree on a lunar albedo of 0.1362 within statistical limits. This gives confidence in both the raster-integration technique and the new CERES calibration parameters, since they are designed to place all instruments on a common SW radiometric scale. This albedo figure is 2.2% higher than that suggested when ROLO simulations are adapted for use within the CERES SW bandpass. However, given the uncertainties in determining thermal radiance leakage of the SW filter and the experimental nature of the calibration used, the absolute accuracy of the CERES measurements presented here is not placed higher than 2–3% (compared to the CERES ERB data accuracy figure of 1%). These results, therefore, do suggest the ROLO simulations across the CERES bandpass also have an average accuracy of the order of $\sim 3\%$ (as opposed to the 5–10% figure assigned to individual wavelength simulations [18]).

This paper also presents what may be the first high-accuracy measurements of lunar thermal output. For very low phase angles the lunar surface emits near to an average 1000 W m^{-2} back to space with a decrease of around 4 W m^{-2} per degree of increasing phase angle. When normalized to 7° phase and 1361 W m^{-2} solar irradiance, measurements of LW flux by the different CERES instruments agree to within the stated CERES 1% accuracy (on an average value of 977 W m^{-2}). This is significant as it suggests that LW ERB measurements by the CERES instruments on the different Terra and Aqua satellites is on the same radiometric scale to within specified accuracy. However, despite the high thermal signal from the Moon, at this point it is not suggested that the LW results presented are at an accuracy higher than the 2–3% figure stated for albedo.

The thermal flux measurements by the CERES WN channels are not of the same absolute accuracy as that proposed for the SW and LW channels due to the narrowband nature of the optics (and lack of knowledge on lunar surface emissivity). However, there is excellent agreement in WN flux between FM1 and FM2, which are located on the same satellite and placed on the same radiometric scale by [8]. This again illustrates both the success of the raster technique and the newly developed CERES calibration.

The operational CERES instruments have now been performing raster scans of the Moon twice every lunar cycle for a little over a year. Subsection 4.B showed that, when the technique presented is applied to such lunar data over the course of a typical

mission, it can act as a check on Total/WN-channel gains. The results suggest that they can be maintained at the 0.3% per decade stability now requested by the climate community [17].

Within an instruments lifetime, the SW lunar data also can be used to assure SW-channel gain stability near to the 0.3% target. Given increased frequency of lunar views, or perhaps higher spatial resolution of future CERES instruments, the signal-to-noise of SW lunar data may be sufficient to reach the target in far less than a decade of measurements. However, given the challenges that may still remain in measuring SW degradation, a new design of ERB instrument solar calibration system is proposed that can use the techniques presented here with raster-scan data of the Sun. This should greatly improve the ability to ensure ERB data accuracy and stability for future missions.

In conclusion, raster-scan measurements of celestial bodies would seem a most useful tool in maintaining calibration of Earth-observing radiometers. This technique is equally applicable for telescopes overfilled by the Moon, such as geostationary imagers and spectrometers, many of which are currently in orbit without onboard calibration systems. Thus, it presents an additional way that the Moon can be used to bring measurements by past and future satellite instruments onto a common radiometric scale. This will significantly improve the length and quality of data vital for use in the climate community.

This work was supported by the NASA Science Mission Directorate. Acknowledgment and appreciation is given to Thomas Stone at the USGS for his assistance in the use of the ROLO model. Special thanks also to Kristen Maglia and Amanda Warner at ITT Visual Information Solutions for support in the use of IDL software.

References

1. S. B. Hooker, W. E. Esaias, G. C. Feldman, W. W. Gregg, and C. R. McClain, "An overview of SeaWiFS and ocean color," Tech. Memo. 104566 (NASA, 1992).
2. R. A. Barnes, R. E. Eplee, F. S. Patt, H. H. Kieffer, T. C. Stone, G. Meister, J. J. Butler, and C. R. McClain, "Comparison of SeaWiFS measurements of the Moon with the U.S. Geological Survey lunar model," *Appl. Opt.* **43**, 5838–5854 (2004).
3. H. H. Kiefer, "Photometric stability of the lunar surface," *Icarus* **130**, 323–327 (1997).
4. B. A. Wielicki, B. R. Barkstrom, E. F. Harrison, R. B. Lee, G. L. Smith, and J. E. Cooper, "Clouds and the Earth's Radiant Energy System (CERES): an Earth observing experiment," *Bull. Am. Meteorol. Soc.* **77**, 853–868 (1996).
5. G. Matthews, K. Priestley, and P. Spence, "Z-domain numerical filter for removal of thermistor bolometer slow mode transients," *Proc. SPIE* **5882**, 588213 (2005).
6. G. Matthews, K. Priestley, N. G. Loeb, K. Loukachine, S. Thomas, D. Walikainen, and B. A. Wielicki, "Coloration determination of spectral darkening occurring on a broadband Earth observing radiometer: application to Clouds and the Earth's Radiant Energy System (CERES)," *Proc. SPIE* **6296**, 62960M (2006).
7. G. Matthews, K. Priestley, and S. Thomas, "Spectral balancing of a broadband earth observing radiometer with co-aligned

- short wave channel to ensure accuracy and stability of broadband daytime outgoing long-wave radiance measurements: application to CERES," Proc. SPIE **6678**, 66781H (2007).
8. G. Matthews, K. Priestley, and S. Thomas, "Transfer of radiometric standards between multiple low Earth orbit climate observing broadband radiometers: application to CERES," Proc. SPIE **6677**, 66770I (2007).
 9. N. G. Loeb, K. J. Priestley, D. P. Kratz, E. B. Geier, R. N. Green, B. A. Wielicki, R. O. Hinton, and S. K. Nolan, "Determination of unfiltered radiances from the Clouds and the Earth's Radiant Energy System instrument," *J. Appl. Meteorol.* **40**, 822–835 (2001).
 10. M. P. A. Haeffelin, J. R. Mahan, and K. J. Priestley, "Predicted dynamic electrothermal performance of thermistor bolometer radiometers for Earth radiation budget applications," *Appl. Opt.* **36**, 7129–7142 (1997).
 11. G. L. Smith, D. K. Pandey, R. B. Lee, B. R. Barkstrom, and K. J. Priestley, "Numerical filtering of spurious transients in a satellite scanning radiometer: application to CERES," *J. Atmos. Ocean. Technol.* **19**, 172–182 (2002).
 12. G. Matthews, K. Priestley, P. Spence, D. Cooper, and D. Walikainen, "Compensation for spectral darkening of short wave optics occurring on the Cloud's and the Earth's Radiant Energy System," Proc. SPIE **5882**, 588212 (2005).
 13. H. Kieffer and T. C. Stone, "The spectral irradiance of the moon," *Astron. J.* **129**, 2887–2901 (2005).
 14. Solar Radiation and Climate Experiment, http://lasp.colorado.edu/sorce/data/tsi_data.htm.
 15. J. W. Salisbury and A. Basu, "Thermal infrared spectra of lunar soils," *Icarus* **130**, 125–139 (1997).
 16. G. Matthews, "CERES science team presentation slide 42" (2007), http://science.larc.nasa.gov/ceres/STM/2007-04/ce0704_240950InstMatthews.pdf.
 17. G. Ohring, B. A. Wielicki, R. Spencer, B. Emery, and R. Datla, "Satellite instrument calibration for measuring global climate change," *Bull. Am. Meteorol. Soc.* **86**, 1303–1313 (2005).
 18. T. C. Stone and H. H. Kiefer, "Use of the moon to support on-orbit sensor calibration for climate change measurements," Proc. SPIE **6296**, 62960Y (2006).